Two-Dimensional Ultrasonic Flaw Detection Based on the Wavelet Packet Transform

Marc C. Robini, Isabelle E. Magnin, *Member, IEEE*, Hugues Benoit-Cattin, and Atilla Baskurt

***Abstract*—An important issue in ultrasonic nondestructive evaluation is the detection of flaw echoes in the presence of coherent background noise associated with the microstructure of materials. Many signal processing techniques have proven to be useful for this purpose, but fully 2-D flaw detection techniques remain desirable. In this paper, we describe a novel automatic flaw detection method based on the wavelet packet transform, which is particularly well adapted to B-scan image analysis. After a brief review of the essential elements of the theory of wavelets and wavelet packets, a detailed description of the method is provided. The detection process operates on a set of spatially oriented frequency channels, i.e., detail images, obtained from successive wavelet packet decompositions of the initial B-scan. A statistical selection procedure based on the modeling of the detail image histograms retains the useful information-bearing frequency channels. The flaw information is then extracted from these selected channels by means of a specific thresholding scheme. Some experimental detection results in B-scan images of austenitic stainless steel samples comprising artificial flaws are presented.**

I. Introduction

Ultrasonic imaging plays an important role in nondestructive evaluation (NDE) of engineering materials as well as in noninvasive diagnostic medicine. However, the detection capability is often severly limited by the interference noise (i.e., clutter, speckle) produced by the unresolvable scatterers randomly distributed throughout the material. Such coherent interference noise may become significant to the point that it completely masks the target of interest (i.e., flaw, tumor, etc.) in both A-scan signals and B-scan images. As a result, a number of techniques have been proposed to improve the signal-to-noise ratio. Typical approaches include spatial compounding [1]–[3], frequency compounding [4], [5], linear bandpass filtering [6], [7] and split-spectrum processing (SSP) techniques such as averaging, minimization, polarity thresholding and Bayesian detection [8]–[12]. In the NDE field, SSP methods give excellent results but can be sensitive to the choice of parameters [13], [14]. Alternative approaches that show less sensitivity to the environment make use of adaptive filtering, order statistic filtering, and constant false-alarm rate detection [15]–[17]. The use of the wavelet transform was also recently considered [18], [19]. When considering B-scan images, fully 2-D flaw detection techniques are desirable whenever the flaw extends over two or more adjacent A-scans, but it appears that few processing techniques perform simultaneously on both dimensions of the image formed [11], [20]–[22]. In the current work, we propose a novel method for automatic 2-D flaw detection based on the wavelet packet transform.

The presence of flaws introduces some modifications of the spectral properties in both directions of the B-scan that can be analyzed separately. In the temporal direction, the physics is governed by the shape of the transmitted sound pulse. If the grain scattering is mainly in the Rayleigh region, the noise spectrum will have most of its power in the high-frequency region of the transducer pass-band [6], [7], [20]. This is not the case for flaw echoes because flaws are generally larger in size than the grain and often behave like geometrical reflectors. In fact, due to the overall filtering effect of attenuation, the flaw spectrum will have a stronger content in the low-frequency region of the transducer pass-band. In the spatial direction, provided that the flaw size is significantly larger than the average grain size of the metal sample being tested, a small shift in the transducer location can result in a significant change of the grain interference pattern, while it has minor effects on the flaw signal [3], [20]. Hence, a relatively flat power spectrum is observed for the time instants corresponding to grain noise only, whereas for the flaw signal, the correlation between the adjacent echoes yields a higher intensity low frequency region [20].

The behavior of the temporal and spatial frequency components of a B-scan image at flaw locations is a productive attribute for detection. Optimal bandpass filtering can provide good results if the information-bearing frequency bands that are dependent on many complex factors (such as the grain size, the flaw size, location and orientation, the scattering properties of the material, the characteristics of the transducer, etc.) are known *a priori*. Yet, in most cases, this information is unknown and alternative flaw detection techniques such as the ones described in [16] and [17] can be used for A-scan processing. When dealing with a B-scan image, one should clearly consider its horizontal (spatial) and vertical (temporal) directions as preferential. Keeping this in mind, the 2-D separable wavelet transform [23], [24], seems to be an effective tool for B-scan processing. However, the conventional wavelet transform decomposes a signal into a set of frequency channels that have narrower bandwidths in the lower frequency region, which makes it suitable for signals consisting pri-

Manuscript received December 13, 1995; accepted March 1, 1997. This work was supported by EDF (Electricité de France) under contract #D12160-08 and has been performed in accordance with the scientific trends of the national research group GDR ISIS of the CNRS (Centre National de la Recherche Scientifique).

The authors are with CREATIS, INSA 502, 69621 Villeurbanne Cedex, France (e-mail: marc.robini@creatis.insa-lyon.fr).

marily of smooth components. This is not directly applicable to bandpass signals such as ultrasonic RF signals and leads naturally to a generalization of the concept of wavelet bases, namely wavelet packets (WP's) [25], [26], which provide the required amount of flexibility to analyze B-scan images.

The design of the flaw detection algorithm proposed in this paper is motivated by the fact that the description of the B-scan in some particular frequency bands (called the useful information-bearing frequency bands) exhibits a stronger flaw-to-clutter ratio (FCR) than the original signal. As suggested above, this assumption holds if the grain scattering is mainly in the Rayleigh region and if the flaw is larger in size than the grain and is intercepted by several adjacent A-scans. Under these conditions, the received wideband B-scan is first partitioned into several sets of independent, spatially oriented frequency channels (detail images) via successive applications of the WP transform, each of these channels being then a potential candidate for flaw detection. Next, a selection of the useful information-bearing frequency channels, that is the channels with the highest FCR, is performed on the basis of the statistics of the detail images, i.e., their probability density functions (PDFs). Appropriate modeling of these PDFs therefore constitutes a key issue of the method. To complete detection, that is to come up with binary results indicating the location of the flaw echoes that are present in the processing window, a global thresholding scheme is employed to extract the flaw information from the high FCR detail images retained by the selection procedure. However, because of the unimodal characteristic of the detail image PDFs, the common threshold selection methods based on the amplitude features are not adapted. Furthermore, due to the varying statistics of the detail images, the thresholds must be set adaptively. Lastly, a simple combination procedure leads to the final detection results.

The paper is organized as follows: in Section II, we briefly review the theory of wavelets and wavelet packets. The application of the WP transform to flaw detection is described in Section III. Section IV presents experimental results for B-scan images of austenitic stainless steel samples (comprising artificial flaws) evaluated with different types of transducers; it appears that the proposed algorithm behaves well in the presence of multiple flaws with different FCR's in the processing window. Concluding remarks are given in Section V.

II. Wavelet Transform and Wavelet Packets

A. A Short Review of Wavelet Analysis

The wavelet transform of a function f corresponds to the decomposition of f on the family of wavelets $(\psi_{a,b}(x))_{a\in\mathbb{R}_+^*,b\in\mathbb{R}}$ generated from one single function ψ (the mother wavelet) by dilatations and translations [23], [27], [28]:

$$\mathrm{WT}_f(a,b) = \int_{-\infty}^{+\infty} f(x)\psi_{a,b}(x)\,dx, \qquad (1)$$

$$\psi_{a,b}(x) = a^{-1/2}\psi\left(\frac{x-b}{a}\right).$$

In practice, one prefers to write f as a discrete superposition corresponding to a discrete set of continuous wavelets. Of particular interest is the discretization on a dyadic grid ($a = 2^j, b = 2^j k, (j,k) \in \mathbb{Z}^2$) for which it is possible to construct functions ψ such that the set $(\psi_{j,k}(x) = 2^{-j/2}\psi(2^{-j}x-k))_{(j,k)\in\mathbb{Z}^2}$ constitutes an orthonormal basis of square integrable functions over $\mathbb{R}$ (i.e., $L^2(\mathbb{R})$) [27]–[30]. On this discrete grid, the wavelet decomposition of f becomes:

$$f(x) = \sum_j \sum_k d_k^j(f)\psi_{j,k}(x) \qquad (2)$$

where the wavelet coefficients $d_k^j(f)$ are inner products of the signal with the wavelet basis functions.

$$d_k^j(f) = \langle f, \psi_{j,k}\rangle = \int_{-\infty}^{+\infty} f(x)\psi_{j,k}(x)\,dx. \qquad (3)$$

This discrete wavelet transform has been extensively studied by Mallat [23], [24], who built a complete mathematical theory of multiresolution analysis particularly well adapted to the use of wavelet bases in image analysis.

In a multiresolution analysis, one considers the set of vector spaces $(V_j)_{j\in\mathbb{Z}}$. These spaces V_j describe successive approximation spaces $\cdots V_2 \subset V_1 \subset V_0 \subset V_{-1} \subset V_{-2} \cdots$ of $L^2(\mathbb{R})$, with resolution 2^{-j}. One also introduces a scaling function ϕ, together with its dilated and translated versions $\phi_{j,k}(x) = 2^{-j/2}\phi(2^{-j}x-k)$, $(j,k) \in \mathbb{Z}^2$, such that $(\phi_{j,k}(x))_{k\in\mathbb{Z}}$ constitutes an orthonormal basis of the closed subspace V_j. For each j, the $\psi_{j,k}$ span a space W_j which is exactly the orthogonal complement in V_{j-1} of V_j. Therefore, the wavelet coefficients $d_k^j(f)$ describe the difference of information between the approximation of f with resolution $2^{-(j-1)}$ and the coarser approximation with resolution 2^{-j}. To construct the mother wavelet ψ, we may first determine the scaling function ϕ which satisfies the two scale difference equation:

$$\phi(x) = \sqrt{2}\sum_n h(n)\phi(2x-n) \qquad (4)$$

where h is the impulse response of a discrete filter defined by $h(n) = 1/2\langle\phi(x/2), \phi(x-n)\rangle, n \in \mathbb{Z}$. The mother wavelet ψ is related to the scaling function via

$$\psi(x) = \sqrt{2}\sum_n g(n)\phi(2x-n) \qquad (5)$$

where $g(n) = (-1)^n h(1-n), n \in \mathbb{Z}$. The algorithm proposed by Mallat [23] for the computation of the $d_k^j(f)$ can

then be summarized by the following two equations:

$$\begin{aligned} d_k^j(f) &= \sum_n g(2k-n)a_n^{j-1}(f) \\ a_k^j(f) &= \sum_n h(2k-n)a_n^{j-1}(f) \end{aligned} \tag{6}$$

where the $a_k^j(f)$ are coefficients characterizing the projection of f onto V_j. If the function f is given in a sampled form, then one can take these samples for the highest order resolution approximation coefficients a_k^0 and (6) describes a subband decomposition on these sampled values with low-pass filter h and high-pass filter g. As originally investigated by Daubechies [27], it is possible to construct orthonormal wavelet bases in which ψ has finite support, therefore corresponding to FIR filters. Much work investigating the design of such filters can be found in the signal processing literature [31]–[34].

An obvious way to extend the 1-D wavelet transform to higher dimensions is to use separable wavelets [23], [24]. Consider a 1-D scaling function $\phi(x)$ and its associated wavelet $\psi(x)$. One can construct four 2-D functions:

$$\begin{aligned} \Phi(x,y) &= \phi(x)\phi(y), \quad \Psi_1(x,y) = \phi(x)\psi(y), \\ \Psi_2(x,y) &= \psi(x)\phi(y), \quad \Psi_3(x,y) = \psi(x)\psi(y), \end{aligned} \tag{7}$$

which are orthogonal to each other with respect to integer shifts. The function $\Phi(x,y)$ is a separable 2-D scaling function (a low pass filter) and the wavelets $\Psi_i(x,y)$ are such that the set $(2^{-j}\Psi_i(2^{-j}x-k, 2^{-j}y-1))_{i=1,2,3;(j,k,l)\in\mathbb{Z}^3}$ is an orthonormal basis of $L^2(\mathbb{R}^2)$. The approximation of a signal $f(x,y)$ at resolution 2^{-j} is characterized by the set of inner products

$$A^j f = \left(\langle f(x,y), 2^{-j}\Phi(2^{-j}x-k, 2^{-j}y-l)\rangle\right)_{(k,l)\in\mathbb{Z}^2}, \tag{8}$$

and the difference of information between $A^{j-1}f$ and the coarser approximation $A^j f$ is given by the detail images

$$D_i^j f = \left(\langle f(x,y), 2^{-j}\Psi_i(2^{-j}x-k, 2^{-j}y-l)\rangle\right)_{(k,l)\in\mathbb{Z}^2}, \quad i=1,2,3. \tag{9}$$

This solution corresponds to a separable 2-D filter bank with subsampling by two in each dimension. Fig. 1 represents one stage in such a decomposition of an image, together with the corresponding partition of the frequency plane. Starting with the function f given in a sampled form $(A^0 f)$, this decomposition scheme is recursively performed to the output giving the low resolution subimage $A^j f$. It leads to the conventional wavelet transform which can be interpreted as an octave band signal decomposition.

B. Wavelet Packets

WP's were introduced by Coifman *et al.* [25] and Wickerhauser [26], as a family of orthonormal bases for discrete functions of $\mathbb{R}^N$, including the wavelet basis and the short-time-Fourier-transform (STFT)-like basis as its members.

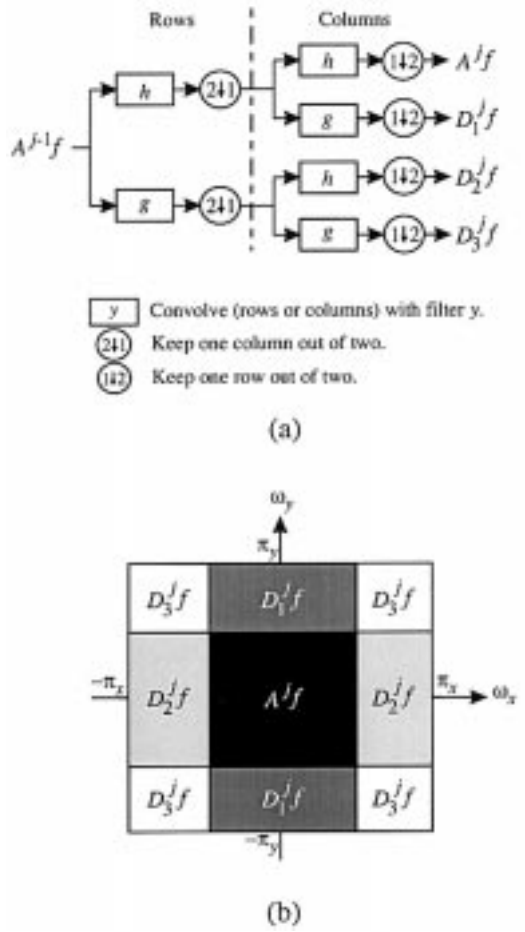

Fig. 1. (a) Separable 2D filter bank corresponding to a separable wavelet basis, the filters h and g are, respectively, a half-band low-pass filter and a half-band highpass filter. $A^{j-1}f$ is the initial image corresponding to resolution $2^{-(j-1)}$, $A^j f$ is the low resolution subimage (2^{-j}), and $(D_i^j)_{i=1,2,3}$ are the detail images corresponding to the information visible at resolution $2^{-(j-1)}$. The corresponding partition of the frequency plane is indicated in (b).

WP's represent a generalization of the method of multiresolution decomposition in the sense that the WP basis functions $(\vartheta_m)_{m\in N}$ can be generated from a given function ϑ_0 according to:

$$\begin{aligned} \vartheta_{2m}(x) &= \sqrt{2}\sum_n h(n)\vartheta_m(2x-n) \\ \vartheta_{2m+1}(x) &= \sqrt{2}\sum_n g(n)\vartheta_m(2x-n) \end{aligned} \tag{10}$$

where the function ϑ_0 can be identified with the scaling function ϕ and ϑ_1 with the mother wavelet ψ. Then, the library of WP bases can be defined to be the collection of orthonormal bases of $L^2(\mathbb{R}^2)$ composed of functions of the form $\vartheta_{j,k,m}(x) = 2^{-j/2}\vartheta_m(2^{-j}x-k), (j,k,m)\in\mathbb{Z}^2\times\mathbb{N}$. Each element of the library is determined by a subset of the indexes j, k, and m (for instance, a conventional wavelet basis corresponds to the collection of indexes $(j,k,1), (j,k)\in\mathbb{Z}^2$). The set $(\vartheta_{j,k,m}(x))_{k\in\mathbb{Z}}$ is an orthonormal basis of a subspace $V_{j,m}$ of $L^2(\mathbb{R})$ such that $V_{j,2m+1}$ is the orthogonal complement of $V_{j,2m}$ in $V_{j-1,m}$, where $V_{j,0}$

can be identified with the closed subspace V_j and $V_{j,1}$ with W_j.

By analogy with (7), one can construct the set of functions

$$(\mathcal{V}_{m,n}(x,y) = \vartheta_m(x)\vartheta_n(y))_{(m,n)\in\mathbb{N}^2}, \tag{11}$$

where $\mathcal{V}_{0,0} = \Phi, \mathcal{V}_{0,1} = \Psi_1, \mathcal{V}_{1,0} = \Psi_2$, and $\mathcal{V}_{1,1} = \Psi_3$ stand as particular cases. A 2-D WP basis is then composed of functions of the form:

$$\mathcal{V}_{j,k,l,m,n}(x,y) = 2^{-j}\mathcal{V}_{m,n}(2^{-j}x - k, 2^{-j}y - 1) \tag{12}$$

where the collection of indexes $(j,k,l,m,n) \in Z^3 \times N^2$ is such that the intervals $\left[2^{-j}m, 2^{-j}(m+1)\right) \times \left[2^{-j}n, 2^{-j}(n+1)\right)$ form a disjoint cover of $[0,+\infty) \times [0,+\infty)$ and k, l range over all the integers. Hence, any triplet $(j,m,n), (m,n) \neq (0,0)$ thus defined gives rise to a detail image:

$$D^j_{m,n}f = (\langle f(x,y), \mathcal{V}_{j,k,l,m,n}(x,y)\rangle)_{(k,l)\in Z^2} \tag{13}$$

which describes $f(x,y)$ in the frequency bands

$$[-(m+1)2^{-j}\pi_x, -m2^{-j}\pi_x] \times [-(n+1)2^{-j}\pi_y, -n2^{-j}\pi_y] \cup [m2^{-j}\pi_x, (m+1)2^{-j}\pi_x] \times [n2^{-j}\pi_y, (n+1)2^{-j}\pi_y].$$

From a practical point of view, the key difference between the conventional wavelet transform and the WP transform is that the decomposition scheme [Fig. 1(a)] is no longer simply applied to the output giving the low frequency subimage. Instead, it can be applied to any output, thus leading to a quadtree structure representation. Let us notice finally that STFT-like bases correspond to the particular case of a regular tree, i.e., when all subimages are decomposed in each scale to achieve full decomposition, or equivalently, uniform frequency resolution.

III. Wavelet Packets Based Ultrasonic Flaw Detection

Due to the separability of the B-scan into orthogonal directions and based on the obervation that its partial spectra (the temporal and spatial frequency components) behave in a distinct manner at flaw locations [3], [6], [7], [20], the 2-D separable wavelet transform appears to be well-suited to B-scan image analysis. The conventional wavelet transform [23], [24], recursively decomposes subsignals in the low frequency channels. However, because the information contained by ultrasonic RF signals is located in the middle frequency channels, further decomposition just in the lower frequency region does not help much for the purpose of flaw detection. Thus, an appropriate way to analyze B-scan images is to allow the decomposition of any frequency channel such as the WP transform [25], [26] does. As we are concerned with detection, redundancy is not prejudicial, it is even desirable. Therefore, we choose to extract the flaw information from the set of detail images $(D^j_{m,n}f)_{j=1,\ldots J; m,n=0,\ldots 2^j-1,(m,n)\neq(0,0)}$ resulting from the decompositions of the initial B-scan A^0f into STFT-like bases of successive depths $1,\ldots J$ (i.e., resolutions $2^{-1},\ldots 2^{-J}$). From a practical point of view, the size of the smallest subimages at resolution 2^{-J} may be used as a stopping criterion for further decomposition. But in order to limit the performance decrease introduced by the resolution loss, we require the numerical period t_c (expressed in pixels) associated with the nominal center frequency f_c of the transducer to be at least one pixel wide at the smallest resolution. Therefore, if f_s denotes the sampling rate for the A-scan signals that constitute the B-scan, then $t_c = f_s/f_c$ has to be such that $2^{-J}t_c \geq 1$ and the stopping criterion is given by:

$$\log_2(f_s/f_c) - 1 < J \leq \log_2(f_s/f_c). \tag{14}$$

TABLE I
8-taps Daubechies Filter Coefficients.

$h(0)$	−0.0535744507090
$h(1)$	−0.0209554825625
$h(2)$	0.3518695343280
$h(3)$	0.5683291217040
$h(4)$	0.2106172671020
$h(5)$	−0.0701588120895
$h(6)$	−0.0089123507210
$h(7)$	0.0227851729480

An example of wavelet packet decompositions of a B-scan into STFT-like bases of depths 1 and 2 is shown in Fig. 2. We used the 8-taps Daubechies filter associated with the "least asymmetric" compactly supported wavelet [27] which normalized coefficients are listed in Table I. The data were collected from an austenitic stainless steel sample with 2 mm diameter holes representing flaws, using a broad-band, focused angle probe (see Section IV for more details: Table III, B-scan #5).

As mentioned earlier, the proposed flaw detection method operates in four steps. A simplified diagram of the process is provided in Fig. 3. The selection of the useful information-bearing frequency channels, to be described in Section III.B, is based on the modeling of the detail image PDFs by generalized Gaussian functions, which is discussed in Section III.A. The adaptive thresholding scheme and the final combination procedure are laid-out in Sections III.C and III.D, respectively.

A. Statistical Properties of Wavelet Coefficients

Because the pixels of the detail images are the decomposition coefficients of the initial image in an orthonormal family, their distribution could exhibit any shape. However, it can be verified in practice that the PDF of the detail images resulting from the decomposition of a B-scan

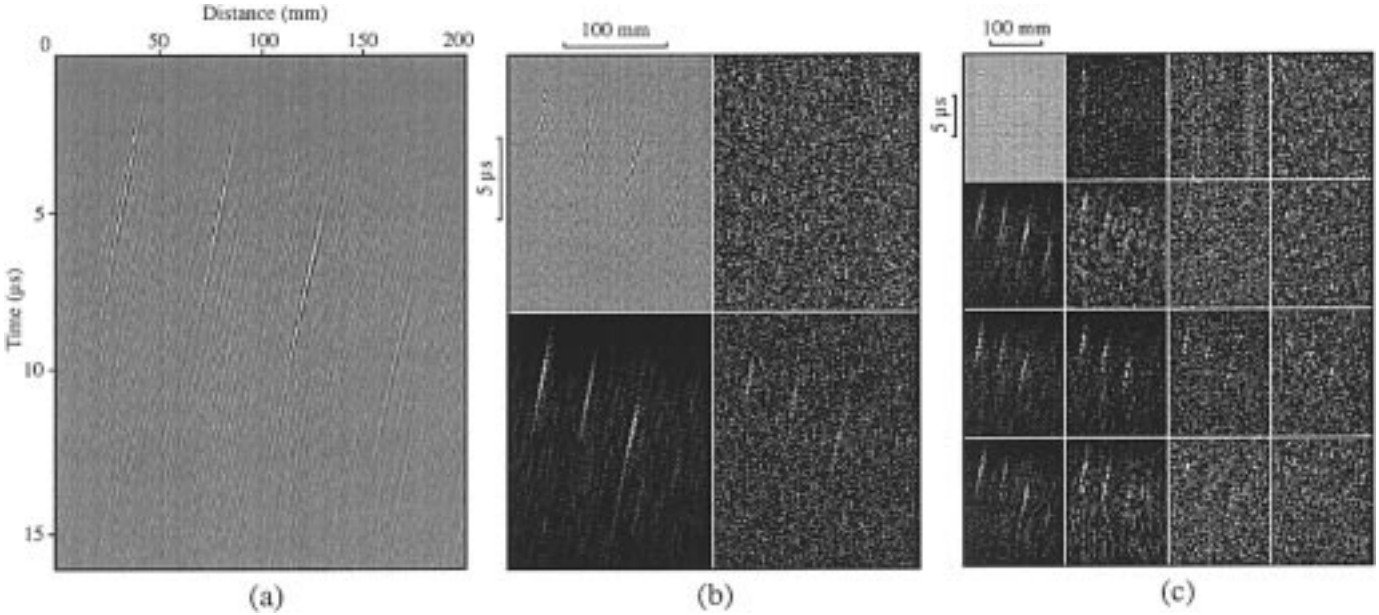

Fig. 2. WP decompositions of a B-scan image (a) (see Section IV and Table III (B-scan #5) for experimental description) into STFT-like bases of depths 1 (b) and 2 (c) (resolutions 2^{-1} and 2^{-2}). According to the scheme presented in Fig. 1(a), the B-scan image is first decomposed into $A^1 f$, $D_1^1 f$, $D_2^1 f$, and $D_3^1 f$, respectively, located in the upper left, upper right, lower left, and lower right quadrant of (b). Each of these four subimages is then decomposed in the same way to obtain the full decomposition of depth 2 and so on. The wavelet coefficients in the detail images are displayed in absolute value, the useful-information-bearing frequency bands appear clearly.

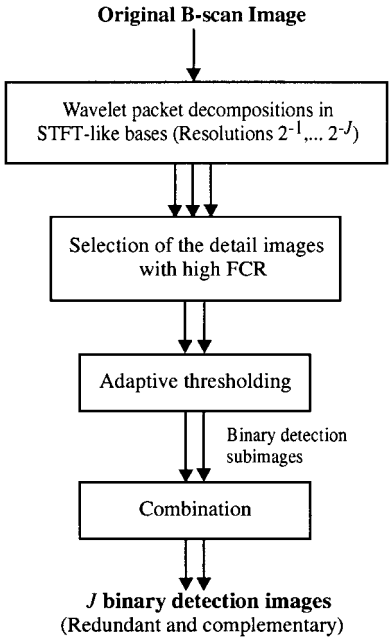

Fig. 3. Principle of the flaw detection method.

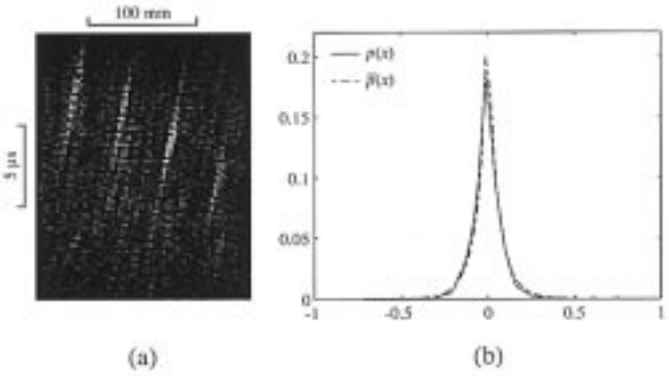

Fig. 4. (a) High FCR detail image resulting from the WP decomposition of depth 2 of the B-scan in Fig. 2. (b) Associated normalized histogram $p(x)$ and its approximation model $\tilde{p}(x)$ (20) ($\alpha = 0.047, \beta = 0.830$).

in a WP basis are symmetrical peaks centered in zero. Indeed, these PDF can be modeled by generalized Gaussian functions, as was already found experimentally in [23] and [35] for other types of signals. The generalized Gaussian law is given by:

$$\tilde{p}(x) = \frac{\beta}{2\alpha\Gamma(1/\beta)} e^{-(|x|/\alpha)^{\beta}} \tag{15}$$

where $\Gamma(.)$ is the standard Gamma function. This is a two-sided symmetric density with two distributional parameters α and β, such that α controls the variance and β modifies the decreasing rate of the central peak. The general formula (15) contains two interesting examples as particular cases: $\beta = 2$ leads to the well-known Gaussian PDF and $\beta = 1$ leads to a Laplacian PDF. The parameters α and β are computed from the mean absolute deviation m_1 and the variance m_2 of the detail image:

$$m_1 = \int_{-\infty}^{+\infty} |x| p(x)\, dx, \quad m_2 = \int_{-\infty}^{+\infty} x^2 p(x)\, dx. \tag{16}$$

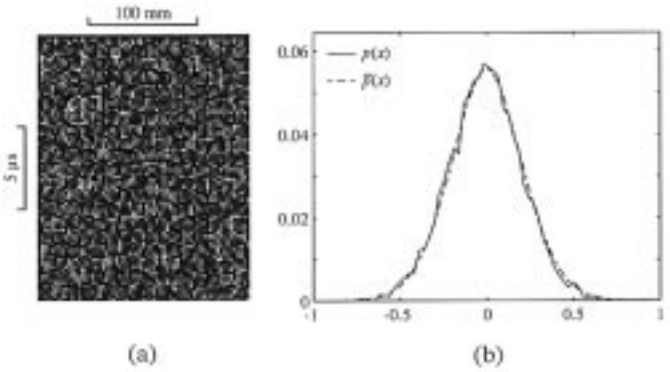

Fig. 5. (a) Grain only detail image resulting from the WP decomposition of depth 2 of the B-scan in Fig. 2. (b) Associated normalized histogram $p(x)$ and its approximation model $\tilde{p}(x)$ (20) ($\alpha = 0.289, \beta = 1.842$).

By replacing the PDF $p(x)$ of the detail image by (15) and changing variables in these two integrals according to:

$$u = \left(\frac{x}{\alpha}\right)^{\beta} \Leftrightarrow dx = \frac{\alpha}{\beta} u^{\frac{1-\beta}{\beta}}\, du, \tag{17}$$

one can derive that

$$m_1 = \alpha \frac{\Gamma(2/\beta)}{\Gamma(1/\beta)} \quad \text{and} \quad m_2 = \alpha^2 \frac{\Gamma(3/\beta)}{\Gamma(1/\beta)}. \tag{18}$$

Thus,

$$\beta = G^{-1}\left(\frac{m_1^2}{m_2}\right), \quad \text{where} \quad G(x) = \frac{\Gamma(2/x)^2}{\Gamma(3/x)\Gamma(1/x)} \tag{19}$$

and α follows directly from either of the two equations in (18). Typical examples of PDF modeling are shown in Figs. 4 and 5.

The quality of the approximation provided by the generalized Gaussian model can be assessed with the help of the measure:

$$V = \max_{-\infty<x<+\infty}(F(x) - \tilde{F}(x)) + \max_{-\infty<x<+\infty}(\tilde{F}(x) - F(x)), \tag{20}$$

which compares two cumulative distribution functions (CDFs) (V is known as the Kuiper's statistic in the literature on goodness-of-fit tests [36], but we use it here as a pure distance measure to show that (15) is a suitable model when dealing with ultrasonic RF signals). In our case, $F(x)$ is estimated from a detail image and $\tilde{F}(x)$ refers to the CDF of its associated PDF model:

$$\tilde{F}(x) = \frac{\beta}{2\alpha\Gamma(1/\beta)} \int_{-\infty}^{x} e^{-(|\nu|/\alpha)^{\beta}}\, d\nu. \tag{21}$$

By changing variables (17), we obtain

$$\tilde{F}(x) = \frac{1}{2}(1 + \text{sign}(x) P\left(1/\beta, (|x|\alpha)^{\beta}\right)) \tag{22}$$

where sign(.) is the signum function and $P(.)$ denotes the incomplete Gamma function,

$$P(a, x) = \frac{1}{\Gamma(a)} \int_{0}^{x} e^{-\nu} \nu^{a-1}\, d\nu, \quad a > 0. \tag{23}$$

Decompositions in STFT-like bases of depths 1, 2, and 3 (that is resolutions 2^{-1}, 2^{-2}, and 2^{-3}, respectively) were applied on six flaw-plus-grain B-scan images obtained with different transducers, using a 8-taps Daubechies wavelet filter (Table I). The PDFs of the resulting detail images were modeled by generalized Gaussian functions (15), (18), (19) and the corresponding distance measures (20) were then computed and averaged for each resolution level. We respectively obtained $E(V) = 0.018$, 0.030 and 0.039 for resolutions 2^{-1}, 2^{-2}, and 2^{-3}, that is 1.8%, 3%, and 3.9% of the dynamic range of the CDFs. These results clearly demonstrate that the generalized Gaussian PDF model (15) is well adapted to the detail image distributions. Also, as suggested by the two examples considered in Figs. 4 and 5, a faster decreasing rate is observed for the PDFs of the detail images with high FCR, which translates to smaller values of the estimated β parameters. To demonstrate this, the high FCR detail images were manually selected and the associated mean β value was found to be 0.770, whereas $E(\beta) = 1.644$ for the remaining low FCR or grain only subimages; meaning, therefore, that the use of β can be very helpful for the selection of the useful information-bearing frequency bands.

B. Selection of the Detail Images

The contents of a detail image with high FCR primarily consists of a majority of low amplitude wavelet coefficients associated with clutter and a few coefficients with significantly higher amplitudes representing flaws. Hence, as shown above, the corresponding PDF exhibits an important decreasing rate such that, for some fixed threshold $T_\beta > 0, \beta \leq T_\beta$ can be used as a first selection criterion. Let us also introduce the measure:

$$m_1(c\sigma) = \int_{-\infty}^{-c\sigma} |x| p(x)\, dx + \int_{c\sigma}^{+\infty} |x| p(x)\, dx \tag{24}$$

where c is a strictly positive constant and $p(x)$ is the PDF of a given detail image with standard deviation σ. Indeed, for normalization purpose, we use the ratio:

$$R_{m_1}(c) = \frac{m_1(c\sigma)}{m_1} = 1 - \frac{1}{m_1} \int_{-c\sqrt{m_2}}^{+c\sqrt{m_2}} |x| p(x)\, dx \tag{25}$$

where m_1 and m_2 are the mean absolute deviation and the variance of the detail image (16), respectively. By inserting (15) of the PDF model and using (18), one can derive that:

$$\tilde{R}_{m_1}(c) = 1 - P(2/\beta, \gamma(c, \beta)) \tag{26}$$

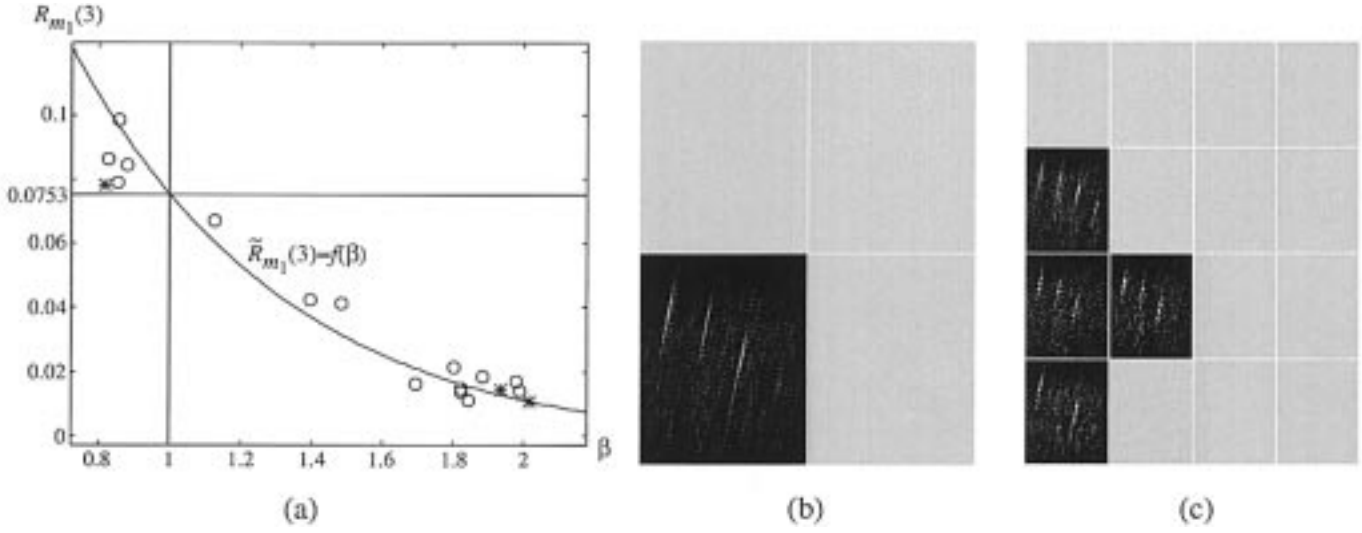

Fig. 6. (a) Repartition of the detail images shown in Fig. 2 in the 2-D parameter space defined by β and $R_{m_1}(3)$ ("$*$" resolution 2^{-1}, "o" resolution 2^{-2}). The selected detail images are located in the upper left quadrant bounded by $\beta = 1$ and $R_{m_1}(3) = 1 - P(2, 3\sqrt{2})$. The corresponding selection results are depicted in (b) and (c) for resolutions 2^{-1} and 2^{-2}, respectively. A careful examination of these results together with Figs. 2(b) and (c) clearly shows that only the detail images containing significant flaw information have been retained.

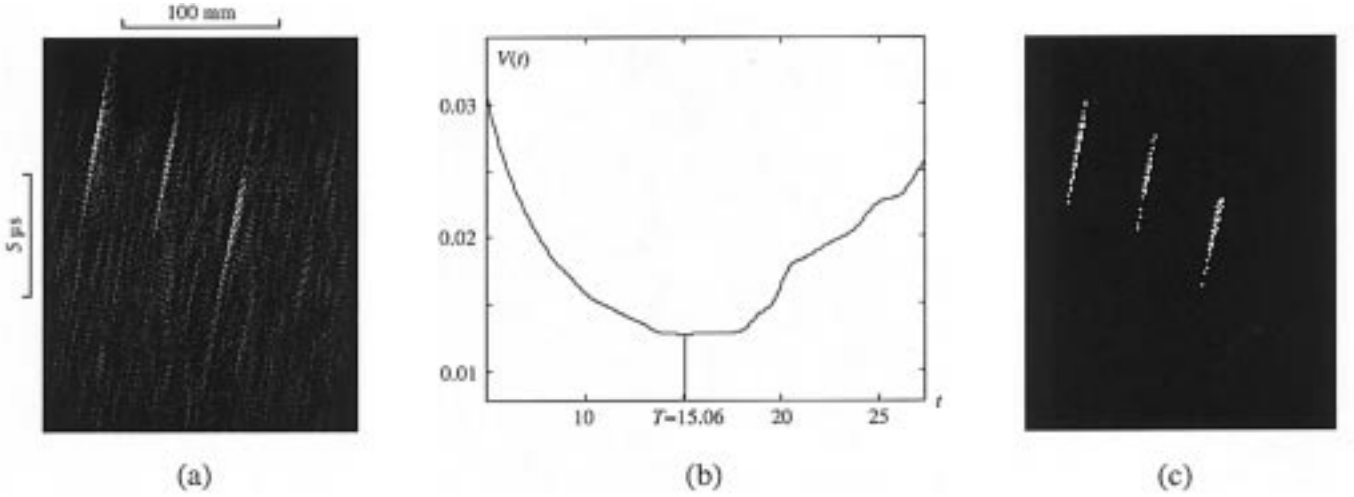

Fig. 7. (a) Detail image resulting from the WP decomposition of depth 1 of the B-scan in Fig. 2 (see Section IV and Table III (B-scan #5) for experimental description) and retained by the selection procedure (36). As depicted in (b), the optimal threshold T is given by the position of the global minimum of the function $V(t)$ (39) derived from the detail image. (c) Binary detection subimage obtained by thresholding with T.

where

$$\gamma(c,\beta) = \left(c \left(\frac{\Gamma(3/\beta)}{\Gamma(1/\beta)} \right)^{1/2} \right)^{\beta} \tag{27}$$

and $P(.)$ is the incomplete Gamma function (23). It appears that $\tilde{R}_{m_1}(c)$ is strictly monotonic, decreasing with respect to β. Thus, if $\beta \leq T_\beta$, one should also verify that $R_{m_1}(c) \geq [\tilde{R}_{m_1}(c)]_{\beta=T_\beta}$. Based on these comments, the selection of the useful information-bearing frequency channels is then achieved by using both the parameter β and the ratio $R_{m_1}(c)$ for complementarity, i.e., any detail image satisfying

$$\begin{cases} \beta \leq T_\beta, \\ R_{m_1}(c) \geq 1 - P\left(2/T_\beta, \gamma(c, T_\beta)\right), \end{cases} \tag{28}$$

will be kept for detection.

When a low FCR or a grain only detail image is observed (Fig. 5), the wavelet coefficients associated with clutter are spread in amplitude, thus leading to a bell-shaped PDF which implies in turn that $\beta > 1$. On the other hand, in the case of a high FCR subimage (Fig. 4), the wavelet coefficients associated with clutter are concentrated in a narrow amplitude interval centered in zero such that the corresponding PDF exhibits a sharp central peak, which translates to $\beta \leq 1$. Hence we set $T_\beta = 1$, a choice

which is also plainly in accordance with the results of the previous subsection. Now, the integration limit (27) can be simplified using the recurrence relation $\Gamma(x+1) = x\Gamma(x)$ and the set of inequalities (28) then becomes:

$$\begin{cases} \beta \leq 1, \\ R_{m_1}(c) \geq 1 - P(2, c\sqrt{2}). \end{cases} \tag{29}$$

Because the threshold connected with $R_{m_1}(c)$ is itself a function of the constant c, efficient selection can be obtained on a continuous interval representing intermediate values of c. As already pointed out, the highest amplitude wavelet coefficients of the high FCR subimages are the ones associated with the flaws. It is, therefore, of major interest to focus on the tails of the distributions. This remark justifies our choice for $c = 3$.

As a consequence, any detail image of the set $(D^j_{m,n}f)_{j=1,\dots J;m,n=0,\dots 2^j-1,(m,n)\neq(0,0)}$ with parameter β (19) and ratio $R_{m_1}(3)$ (25) satisfying

$$\begin{cases} \beta \leq 1, \\ R_{m_1}(3) \geq 1 - P(2, 3\sqrt{2}) \approx 0.0753 \end{cases} \tag{30}$$

will be thresholded using the adaptive scheme to be described next. Fig. 6(a) gives an example of the repartition of some detail images in the $(\beta, R_{m_1}(3))$ plane together with a plot of $\tilde{R}_{m_1}(3)$ versus β. The detail images considered here result from the decompositions in STFT-like bases of depths 1 and 2 of the B-scan image in Fig. 2. The corresponding selection results are shown in Fig. 6(b) and (c), respectively.

C. Thresholding of the Detail Images

The detail images $(D^j_{m,n}f)_{j=1,\dots J;m,n\in 0,\dots 2^j-1}$ retained by the selection procedure (30) exhibit high FCR, which means that a global thresholding scheme can be employed to come up with the binary flaw detection results. Let us denote a detail image $D^j_{m,n}f$ of size $M_j \times N_j$ by the set X of M_jN_j wavelet coefficients: $X = \{X(k,l); k = 0, \dots M_j - 1, l = 0, \dots N_j - 1\}$. This set can be viewed as the union of two subsets X_f and X_c, where X_f contains the wavelet coefficients associated with the flaws and X_c corresponds to the background of the subimage (the wavelet coefficients associated with clutter):

$$X = X_f \cup X_c$$

where

$$X_f = \{X(k_f, l_f)\}, \quad X_c = \{X(k_c, l_c)\},$$
$$(k_f, l_f) \neq (k_c, l_c)$$
$$\forall (k_f, l_f), (k_c, l_c) \in \{0, \dots M_j - 1\} \times \{0, \dots N_j - 1\}.$$

The problem is then to derive a partition of X approaching the ideal partition (X_f, X_c). Because of the unimodal characteristic of the detail images histograms, threshold selection is not a simple task and it must be supported by some hypotheses:

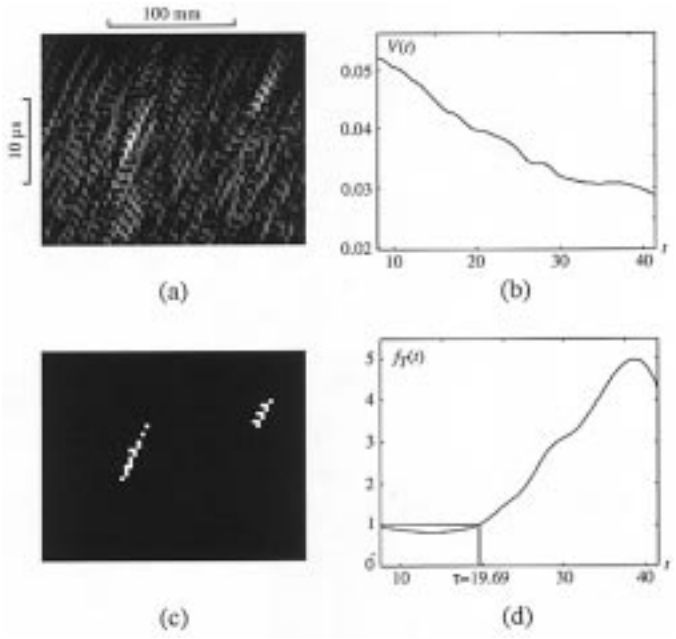

Fig. 8. (a) Detail image obtained from the WP decomposition of depth 2 of the B-scan in Fig. 12 (see Section IV and Table III (B-scan #6) for experimental description) and corresponding to a borderline case of selection. As shown in (b), the corresponding function $V(t)$ (31) does not exhibit a global minimum, and the optimal threshold T cannot be derived. (c) Function $f_T(t) = m_1(t)/\tilde{m}_1(t)$ derived from the detail image, we set the threshold to the value τ satisfying $f_T(\tau) = 1$. (d) Binary detection subimage obtained by thresholding with τ.

- H_1: There exists an optimal threshold T such that the elements of X_f and X_c satisfy $|X(k_c, l_c)| \leq T$ and $|X(k_f, l_f)| > T$.
- H_2: The wavelet coefficients $X(k_f, l_f)$ associated with the flaws create some imbalance in the statistics of the detail image X, resulting in a degradation of its PDF approximation (15).

Hypothesis H_1 is necessary to ensure that a solution exists for the extraction of flaw information through global thresholding. Additionally, hypothesis H_2 also may be formulated as follows: of any subset included in X, the subset X_c of wavelet coefficients associated with clutter leads to the best-fitted PDF approximation with a generalized Gaussian law. In order to prove this, consider a subset $X(t)$ of X defined by $X(t) = \{X(k,l) \in X; |X(k,l)| \leq t\}$ and let $p_{(t)}(.)$ be the distribution of the elements of this subset. The accuracy of the approximation provided by the corresponding PDF model $\tilde{p}_{(t)}(.)$ can be assessed by the distance measure

$$V(t) = \max_{-\infty<x<+\infty} \left(F_{(t)}(x) - \tilde{F}_{(t)}(x) \right) + \max_{-\infty<x<+\infty} \left(\tilde{F}_{(t)}(x) - F_{(t)}(x) \right) \tag{31}$$

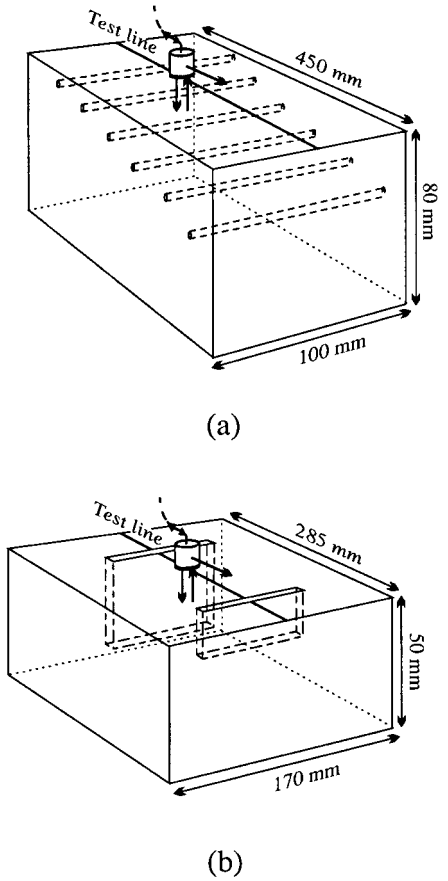

Fig. 9. Experimental set-up. B-scan images were recorded from two austenitic stainless-steel samples with 1 mm mean grain diameter and comprising artificial flaws. The first sample (a) contains 2 mm diameter holes parallel to the control surface and located at different depths. The second sample (b) contains two open notches 0.3 mm thick. Each B-scan consists of equally spaced (0.8 mm) A-scans positioned along a straight line, and the measurements were performed in immersion using the transducers presented in Table II (see Table III for further description).

where $F_{(t)}(.)$ is the CDF estimated from the elements of $X(t)$, that is

$$F_{(t)}(x) = \int_{-\infty}^{x} p_{(t)}(\nu)\, d\nu,$$

and $\tilde{F}_{(t)}(.)$ refers to the associated CDF model (22). Then, if the two hypotheses H_1, H_2 are to be satisfied, $V(t)$ reaches a global minimum when the parameter t is equal to the optimal threshold:

$$T = \arg\min_{t>0} V(t). \tag{32}$$

An example of a result obtained with this method is given in Fig. 7. As for many other examples, the flaw information contents are successfully extracted, which therefore validates the two hypotheses.

However, in practice, the distance measure (31) may not be sensitive enough to cope with limit cases of selection (30) corresponding to detail images with lower FCR or with a set X_f of very low cardinality. Therefore, in order to increase sensitivity, we use a measure based on the first moment rather than the distribution itself:

$$m_1(t) = \int_{-\infty}^{-t} |x| p(x)\, dx + \int_{t}^{+\infty} |x| p(x)\, dx. \tag{33}$$

By inserting (15) of the PDF model and changing variables (17), one can derive that

$$\tilde{m}_1(t) = \alpha \frac{\Gamma(2/\beta)}{\Gamma(1/\beta)} \left(1 - P(2/\beta, (t/\alpha)^{\beta})\right), \tag{34}$$

and it follows from hypotheses H_1 and H_2 that

$$\begin{cases} m_1(t) \le \tilde{m}_1(t) & \text{if } t \le \tau \approx T, \\ m_1(t) > \tilde{m}_1(t) & \text{if } t > \tau \approx T, \end{cases} \tag{35}$$

(Note that because of the discrete nature of the detail images, the second inequality does not hold for $t \gg T$). Global threshold selection is then given by:

$$\tau = \arg\min_{t>0} |m_1(t) - \tilde{m}_1(t)| \approx T, \tag{36}$$

which is equivalent to select the value of the parameter t such that the function $f_T(t) = m_1(t)/\tilde{m}_1(t)$ is equal to one, i.e. $f_T(\tau) = 1, \tau \approx T$.

The gain in sensitivity achieved by this last method, as depicted in Fig. 8, constitutes its first advantage. Moreover, when compared with (32), which involves the computation of some PDF model parameters and the estimation of a CDF for each t, this method appears to be far less time consuming. Consequently, global threshold selection using (36) is systematically employed. Thresholding the detail images $(D^j_{m,n} f)_{j=1,\dots J; m,n \in 0,\dots 2^j-1}$ retained by the selection procedure (30) leads to the set $(B^j_{m,n})_{j=1,\dots J; m,n \in 0,\dots 2^j-1}$ of binary detection subimages defined by:

$$B^j_{m,n}(k,l) = \begin{cases} 1 & \text{if } |D^j_{m,n} f(k,l)| \ge \tau^j_{m,n}, \\ 0 & \text{otherwise,} \end{cases} \tag{37}$$

where $\tau^j_{m,n}$ is the threshold associated to $D^j_{m,n} f$.

D. Combination of the Binary Detection Subimages

The last step of the method consists in appropriately combining the binary detection subimages resulting from the above thresholding procedure to obtain the final detection result. Because the detection scheme operates on the detail images resulting from the WP decompositions of the initial B-scan into STFT-like bases of depths $1, \dots J$ (resolutions $2^{-1}, \dots 2^{-J}$), we choose to apply separately the same combination process to the binary detection subimages corresponding to each resolution level. This leads to J binary detection images, both redundant and complementary. Redundancy is observed as soon as two binary detection subimages located at different resolution levels correspond to overlapping frequency channels. Conversely,

TABLE II
TRANSDUCERS USED IN THE EXPERIMENTS.

CD-2-15 (Sonatest)	2 MHz	0°	Narrow-band, Unfocused.
SEB1 (Krautkrämer)	1 MHz	0°	Narrow-band, Unfocused.
TS45-1-425 (Vinçotte)	1 MHz	45°	Broad-band, focused.
TS60-2-345 (Vinçotte)	2 MHz	60°	Broad-band, focused.
TS70-2-325 (Vinçotte)	2 MHz	70°	Broad-band, focused.

complementarity arises when a frequency channel associated with a given binary detection subimage do not overlap any other useful information-bearing frequency band in another resolution level.

For combining the flaw information in the binary detection subimages at a same resolution level $2^{-j}, j \in 1, \ldots J$, we propose the following method: all subimages $(B^j_{m,n})_{m,n\in 0,\ldots 2^j-1}$ are first combined through a logical OR operation, which leads to a single binary detection subimage B^j. Next, the subimage B^j of size $M_j \times N_j = (M/2^j) \times (N/2^j)$ is brought back to the size $M \times N$ of the initial B-scan by iterative upsampling followed by low-pass filtering. A closing operation (dilatation followed by erosion) [37] is applied on each temporal direction of the resulting binary detection image, say $B^j_{M\times N}$, using a flat structuring element of width f_s/f_c where f_c denotes the nominal center frequency of the transducer and f_s is the sampling rate for the A-scan acquisitions. This morphological filtering operation allows to fuse the nonsignificant gaps of width smaller than half the numerical period t_c defined by the dominant frequency f_c of the ultrasonic RF signals that constitute the B-scan.

IV. EXPERIMENTAL RESULTS

Experiments have been conducted on two austenitic stainless-steel samples with equiaxed grains of about 1 mm in diameter. In the first sample [Fig. 9(a)], the flaws were formed by drilling 2 mm diameter holes parallel to the surface at a depth of between 2.5 and 30 mm. The second sample [Fig. 9(b)] contains two open notches of different depths, 0.3 mm thick, fabricated by electro-erosion. Seven B-scan images (five for the first sample and two for the second sample) were obtained by combining A-scan signals recorded for equally spaced (0.8 mm) transducer locations along a test line. The measurements were performed in immersion, using five different types of transducers (three of which are angle probes), either broad-band and focused or narrow-band and unfocused, and with nominal center frequency equal to 1 or 2 MHz, as summarized in Table II. The signals were digitized on 8 bits using a LeCroy 9450 oscilloscope, with a sampling frequency of 10 or 20 MHz depending on the center frequency of the transducer. This description is completed by Table III, where the peak FCR

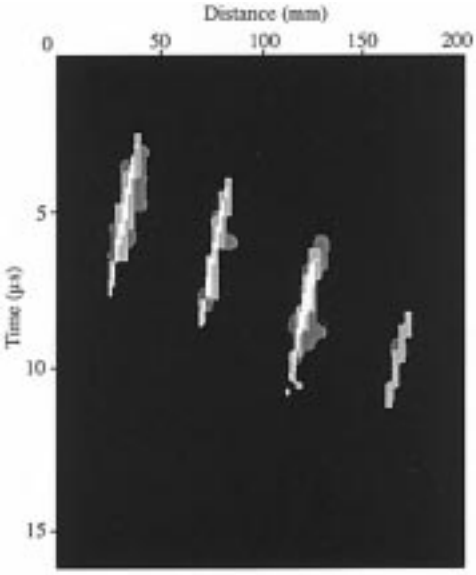

Fig. 10. Flaw detection result for the B-scan image in Fig. 2 (Table III, B-scan #5). The binary detection images corresponding to the different resolution levels are superimposed using different gray level amplitudes.

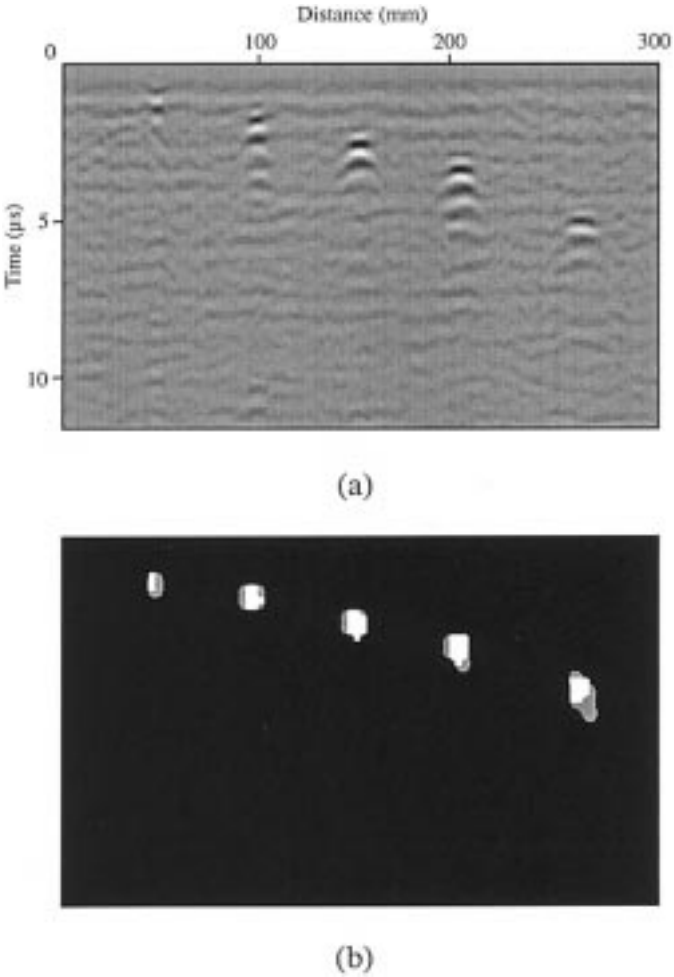

Fig. 11. (a) Experimental B-scan image of five holes drilled in an austenitic stainless steel block (Table III, B-scan #2). (b) Flaw detection result.

TABLE III

RESULTS OF EXPERIMENTS CONDUCTED ON AUSTENITIC STAINLESS STEEL SAMPLES COMPRISING ARTIFICIAL FLAWS. EACH B-SCAN WAS OBTAINED BY COMBINING A-SCANS RECORDED FOR EQUALLY SPACED (0.8 MM) TRANSDUCER LOCATIONS ALONG A STRAIGHT LINE (FIG. 9).

	B-scan #1	B-scan #2	B-scan #3	B-scan #4	B-scan #5	B-scan #6	B-scan #7
Type of flaws	2mm-$\emptyset$ holes	2mm-$\emptyset$ holes	2mm-$\emptyset$ holes	2mm-$\emptyset$ holes	2mm-$\emptyset$ holes	Open notches	Open notches
Transducer	CD-2-15	SEB1	TS45-1-425	TS60-2-345	TS70-2-325	TS45-1-425	TS60-2-345
Sampling rate	20 MHz	10 MHz	10 MHz	20 MHz	20 MHz	10 MHz	20 MHz
A-scans $\times$ samples	464×506	376×226	390×250	323×506	253×321	257×250	252×506
# of flaw echoes	6	5	6	6	4	2	2
Peak FCR values	1.3, 3.5, 4.5, 4.2, 2.8, 1.5	2.3, 3.1, 3.25, 3.1, 2.15	$(<1), \approx 1$, 2.5, 4.5, 5.8, 3.2	≈ 1, 1.7, 3.3, 2.9, 1.8, ≈ 1	3.0, 2.25, 2.5, ≈ 1	1.3, 2.0	2.0, 1.5
Detected flaw echoes	6	5	5	6	4	2	2

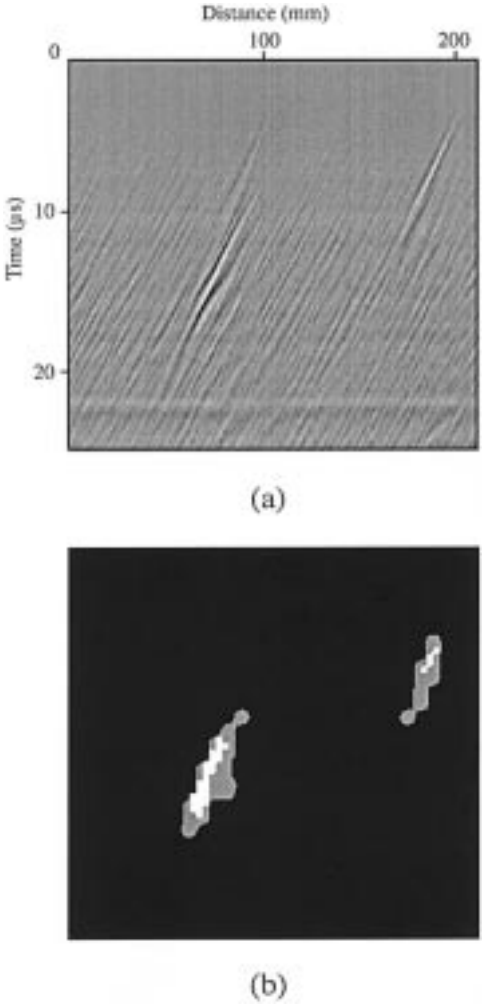

Fig. 12. (a) Experimental B-scan image of two open notches fabricated by electro-erosion in an austenitic stainless steel block (Table III, B-scan #6). (b) Flaw detection result.

values of the flaw echoes present in each B-scan can also be found (for a given flaw, the peak FCR is defined as the ratio between the highest peak amplitude associated with the flaw and the highest peak amplitude associated with the surrounding grain echoes). For all the cases reported in this table, the ratio f_s/f_c is equal to 10, which implies that the lowest resolution considered is 2^{-3}, according to (14).

Let us first consider the B-scan image shown in Fig. 2(a) (B-scan #5 in Table III), collected from the austenitic stainless steel sample containing holes with a broad-band, focused angle probe (TS70-2-325, 2 MHz, Vinçotte) generating transverse waves at 70°. Four flaw echoes associated with holes located at depths 2.5, 5, 10, and 15 mm into the sample are detectable in this image and the corresponding peak FCR values (from left to right) are 3.0, 2.25, 2.5, and 1.0. The detection result is displayed in Fig. 10 as follows: the binary detection images corresponding to the three resolution levels are simply superimposed using different grey level amplitudes, the lower amplitudes being associated with the lower resolution levels. The four flaw echoes were accurately detected, as reported in Table III. As could be expected, the lower the resolution, the coarser the shape of the detection result is. More precisely, taking the spatial resolution of the original B-scan to be equal to 1 (in relative units), the spatial resolution of the flaw detection method ranges beetween 2^{-1} and 2^{-J}, depending on the depth of decomposition where the detail images retained by the selection procedure are to be located. However, this does not constitute a negative attribute for the purpose of detection because good localization is observed. One can also notice that the flaw echo with lowest FCR was not detected at resolution 2^{-1}, which provides motivation for redundant WP decompositions of successive depths.

A B-scan of the first sample (Table III, B-scan #2) is also considered in Fig. 11. It was obtained by using an unfocused transducer (SEB1, Sonatest) with a nominal center frequency of 1 MHz. The peak FCR values associated with the five flaw echoes are 2.3, 3.1, 3.25, 3.1, and 2.15 (from left to right). The detection result [Fig. 11(b)] corresponds to the useful information-bearing frequency channels that were found at resolutions 2^{-2} and 2^{-3}. In fact,

the selection procedure did not retain any detail image at resolution 2^{-1}, thus underlying again the need for redundant WP decompositions. The B-scan shown in Fig. 12 (Table III, B-scan #6) was obtained from the sample containing open notches, by using a broadband, focused transducer (TS45-1-425, 1 MHz, Vinçotte) generating transverse waves at 45°. Here, the lower ends of two notches 5 and 20 mm deep are detectable through their diffraction echo, with peak SNR values respectively equal to 1.3 and 2. We obtained good detection for both of them; and, as for the previous example, no useful information-bearing frequency channel was found at resolution 2^{-1}.

All the flaw echoes that are visually detectable by an operator have been correctly detected without any false alarm for the examples reported in Table III. Hence, it comes up that the proposed detection method is not sensitive to the choice of the transducer and to the presence of multiple flaws with different FCRs in the processing window, which tends to prove that it may be well adapted to varying testing environments. Finally, let us mention that real time implementation is not conceivable by that time. However, it does not appear to be too time consuming. For instance, the total amount of time required to process the B-scan images presented here ranges between 10 and 20 seconds on a Digital 3000/300X alpha workstation.

V. Conclusion

We have presented a novel ultrasonic flaw detection method in ultrasonic NDE B-mode scans. The detection process operates on the set of spatially oriented frequency channels (i.e., the detail images) obtained from the WP decompositions of the initial B-scan into STFT-like bases of successive depths. Based on an appropriate modeling of the detail image histograms, we designed an effective procedure for the selection of the useful information-bearing frequency channels in order to facilitate the flaw information extraction by means of an adaptive thresholding scheme. A specific combination process has been proposed to come up with the final detection result, that is a set of binary detection images (both redundant and complementary) corresponding to the different resolution levels. This method is fully two-dimensional and the detection results obtained on artificial flaws with different types of transducers proved its reliability. Furthermore, it is truly automatic since the required knowledge about the testing environment simply consists in the nominal center frequency of the transducer and the sampling rate for the A-scan signals that constitute the B-scan, both of which are known in most cases. This detection method can be of great help to the qualified operator in order to perform pertinent flaw detection. Because it is automatic and not too time consuming, it may be systematically employed for the analysis of large volumes of data in the nondestructive evaluation field. Finally, note that the three-dimensional extension of the method is relatively straightforward, which makes it even more suitable for real industrial applications.

Acknowledgments

The authors would like to thank B. Georgel and C. Cloarec for their contribution to this work.

References

[1] G. E. Trahey, S. W. Smith, and O. T.Von Ramm, "Speckle pattern correlation with lateral aperture translation: Experimental results and implications for spatial compounding," *IEEE Trans. Ultrason., Ferroelect., Freq. Contr.*, vol. 33, no. 3, pp. 257–264, 1986.

[2] P. M. Shankar, "Speckle reduction in ultrasound B-scans using weighted averaging in spatial compounding," *IEEE Trans. Ultrason., Ferroelect., Freq. Contr.*, vol. 33, no. 6, pp. 754–758, 1986.

[3] N. M. Bilgutay, R. Murthy, U. Bencharit, and J. Saniie, "Spatial processing for coherent noise reduction in ultrasonic imaging," *J. Acoust. Soc. Amer.*, vol. 87, no. 2, pp. 728–736, 1990.

[4] H. E. Melton and P. A. Magnin, "A-mode speckle reduction with compound frequencies and compound bandwidths," *Ultrason. Imaging*, vol. 6, pp. 159–173, 1984.

[5] I. Amir, N. M. Bilgutay, and V. L. Newhouse, "Analysis and comparison of some frequency compounding algorithms for the reduction of ultrasonic clutter," *IEEE Trans. Ultrason., Ferroelect., Freq. Contr.*, vol. 33, no. 4, pp. 402–411, 1986.

[6] P. M. Shankar, U. Bencharit, N. M. Bilgutay, and J. Saniie, "Grain noise suppression through bandpass filtering," *Mater. Eval.*, vol. 46, pp. 1100–1104, July 1988.

[7] R. Murthy, N. M. Bilgutay, and J. Saniie, "Application of bandpass filtering in ultrasonic non-destructive testing," *Quantitative Nondestructive Eval. Mater.*, vol. 8, pp. 759–767, 1989.

[8] V. L. Newhouse, N. M. Bilgutay, J. Saniie, and E. S. Furgason, "Flaw-to-grain echo enhancement by split-spectrum processing," *Ultrasonics*, vol. 20, pp. 59–68, Mar. 1982.

[9] J. L. Rose, P. Karpur, and V. L. Newhouse, "Utility of split-spectrum processing in ultrasonic nondestructive evaluation," *Mater. Eval.*, vol. 46, pp. 114–121, Jan. 1988.

[10] P. M. Shankar, P. Karpur, V. L. Newhouse, and J. L. Rose, "Split-spectrum processing: analysis of polarity thresholding algorithm for improvement of signal-to-noise ratio and detectability in ultrasonic signals," *IEEE Trans. Ultrason., Ferroelect., Freq. Contr.*, vol. 36, no. 1, pp. 101–108, 1989.

[11] N. M. Bilgutay, U. Bencharit, R. Murthy, and J. Saniie, "Analysis of a non-linear frequency diverse clutter suppression algorithm," *Ultrasonics*, vol. 28, pp. 90–96, Mar. 1990.

[12] J. Saniie, T. Wang, and X. Jin, "Performance evaluation of frequency diverse Bayesian ultrasonic flaw detection," *J. Acoust. Soc. Amer.*, vol. 91, no. 4, pp. 2034–2041, 1992.

[13] P. Karpur, P. M. Shankar, J. L. Rose, and V. L. Newhouse, "Split-spectrum processing: optimizing the parameters using minimization," *Ultrasonics*, vol. 25, pp. 204–208, July 1987.

[14] P. Karpur, P. M. Shankar, J. L. Rose, and V. L. Newhouse, "Split-spectrum processing: Determination of the available bandwidth for spectral splitting," *Ultrasonics*, vol. 26, pp. 204–209, July 1988.

[15] Y. Zhu and P. Weight, "Ultrasonic nondestructive evaluation of highly scattering materials using adaptive filtering and detection," *IEEE Trans. Ultrason., Ferroelect., Freq. Contr.*, vol. 41, no. 1, pp. 26–33, 1994.

[16] J. Saniie, D. T. Nagle, and K. D. Donohue, "Analysis of order statistic filters applied to ultrasonic flaw detection using split-spectrum processing," *IEEE Trans. Ultrason., Ferroelect., Freq. Contr.*, vol. 38, no. 2, pp. 133–140, 1991.

[17] J. Saniie and D. T. Nagle, "Analysis of order-statistic CFAR threshold estimators for improved ultrasonic flaw detection," *IEEE Trans. Ultrason., Ferroelect., Freq. Contr.*, vol. 39, no. 5, pp. 618–630, 1992.

[18] A. Abbate, J. Koay, J. Frankel, S. C. Schroeder, and P. Das, "Application of wavelet transform signal processor to ultrasound," *Proc. IEEE Ultrason. Symp.*, 1994, pp. 1147–1152.

[19] K. Kaya, N. M. Bilgutay, and R. Murthy, "Flaw detection in stainless steel samples using wavelet decomposition," *Proc. IEEE Ultrason. Symp.*, 1994, pp. 1271–1274.

[20] R. Murthy, N. M. Bilguthay, and X. Li, "Temporal and spatial spectral features of B-scan images," *Proc. IEEE Ultrason. Symp.*, 1991, pp. 799–802.
[21] J. Moysan, G. Corneloup, I. E. Magnin, and P. Benoist, "Crack-like defect detection and sizing from image segmentation through co-occurrence matrix analysis," *Ultrasonics*, vol. 30, no. 6, pp. 359–363, 1992.
[22] J. Moysan, G. Corneloup, I. E. Magnin, and P. Benoist, "Matrice de co-occurrence optimale pour la segmentation automatique d'images ultrasonores," *Traitement du Signal*, vol. 9, no. 4, pp. 309–323, 1992.
[23] S. Mallat, "A theory for multiresolution signal decomposition: The wavelet representation," *IEEE Trans. Pattern Anal. Machine Intell.*, vol. 11, no. 7, pp. 674–693, 1989.
[24] S. Mallat, "Multiresolution approximations and wavelet orthonormal bases of $L^2(R)$," *Trans. Amer. Math. Soc.*, vol. 315, no. 1, pp. 69–87, 1989.
[25] R. Coifman, Y. Meyer, S. Quaker, and V. Wickerhauser, "Signal processing and compression with wave packets," Tech. Rep., Dept. Math., Yale University, New Haven, Connecticut, 1990, available from ftp.math.yale.edu in /pub/wavelets/papers/cmqw.tex.
[26] M. V. Wickerhauser, "Acoustic signal compression with wavelet packets," in *Wavelets: A Tutorial in Theory and Applications*, C. K. Chui, Ed., New York: Academic, 1992, pp. 679–700.
[27] I. Daubechies, "Orthonormal bases of compactly supported wavelets," *Commun. Pure Appl. Math.*, vol. XLI, pp. 909–996, 1988.
[28] Y. Meyer, "Orthonormal wavelets," in *Wavelets, Time-Frequency Methods and Phase Space* (Lecture Notes on IPTI), J. M. Combes *et al.*, Eds. New York: Springer-Verlag, 1989, pp. 21–37.
[29] P. B. Lemarié, "Une nouvelle base d'ondelettes de $L^2(\mathbb{R})$," *J. Math. Pures Appl.*, vol. 67, pp. 227–238, 1988.
[30] G. Battle, "A block spin construction of wavelets. Part I. Lemarié functions," *Commun. Math. Phys.*, vol. 110, pp. 601–615, 1987.
[31] F. Mintzer, "Filters for distorsion free two-band multirate filter banks," *IEEE Trans. Acoust., Speech, Signal Processing*, vol. ASSP-33, pp. 626–630, 1985.
[32] M. J. T Smith and T. P. Barnwell, "Exact reconstruction techniques for tree-structured subband coders," *IEEE Trans. Acoust., Speech, Signal Processing*, vol. ASSP-34, pp. 434–441, 1986.
[33] M. Vetterli, "Filter banks allowing perfect reconstruction," *Signal Process.*, vol. 10, no. 3, pp. 219–244, 1986.
[34] O. Rioul and P. Duhamel, "A remez exchange algorithm for orthonormal wavelets," *IEEE Trans. Circuits Syst. II*, vol. 41, no. 8, pp. 550–560, 1994.
[35] M. Antonini, M. Barlaud, P. Mathieu, and I. Daubechies, "Image coding using vector quantization in the wavelet transform domain," *Proc. IEEE ICASSP*, pp. 2297–2300, 1990.
[36] M. A. Stephens, "EDF statistics for goodness of fit and some comparisons," *J. Amer. Stat. Assoc.*, vol. 69, no. 347, pp. 730–737, 1974.
[37] R. M. Haralick, S. R. Stenberg, and X. Zhuang, "Image analysis using mathematical morphology," *IEEE Trans. Pattern Anal. Machine Intell.*, vol. 9, no. 4, pp. 532–550, 1987.

Marc C. Robini was born in Cannes, France, on April 13, 1971. He received his B.S. degree in electrical engineering from the National Institute of Applied Sciences (INSA) of Lyon, France, in 1993.

He is currently a Ph.D. student at the CREATIS (Research Unit Associated with CNRS (UMR 5515) and affiliated to INSERM, Lyon, France). His current research interests include image processing applications in the NDE field, inverse problems, and dynamic Monte Carlo methods.

Isabelle E. Magnin (M'85) received the engineering degree from the Ecole Catholique des Arts et Metiers (ECAM), Lyon, France, the doctor engineer degree (1981) and the "Doctorat ès Sciences" (1987) from the National Insitute of Applied Sciences (INSA) of Lyon.

Since 1982, she has been a researcher with the National Institute for Health and Medical Research (INSERM) at the CREATIS, Lyon, France. Her main interests concern 2-D and 3-D image processing, multiresolution approaches, and deformable models.

Hugues Benoit-Cattin received his B.S. degree in electrical engineering from the National Institute of Applied Sciences (INSA) of Lyon, France, in 1992. He received his Ph.D. degree in image processing from INSA in 1995.

His research interests include multidimensional image processing, wavelet analysis, and image coding.

Atilla Baskurt received his B.S. degree in electrical engineering from the National Institute of Applied Sciences (INSA) of Lyon, France, in 1984. He received his M.S. and Ph.D. degrees in computer science from INSA, in 1985 and 1989.

He is currently Maître de Conférences at the CREATIS (Research Unit associated with CNRS (UMR 5515) and affiliated to INSERM) and in the Departement of Electrical Engineering of INSA. His research interests include multidimensional image processing, wavelet analysis, and image coding.